Journal of Materials Science & Technology 250 (2026) 205–218

Contents lists available at ScienceDirect

Journal of Materials Science & Technology

journal homepage: www.elsevier.com/locate/jmst

Research Article

Hard yet tough Ti/TiAlN multilayer coatings: Erosion resistance and micropillar compression

Jingjun Yan[a,b], Yan Zhang[a], Yupeng Zhang[a], Guanshui Ma[a], Shenghao Zhou[a], Zhenyu Wang[a,*], Aiying Wang[a,b,*]

[a] State Key Laboratory of Advanced Marine Materials, Zhejiang Key Laboratory of Extreme-environmental Material Surfaces and Interfaces, Ningbo Institute of Materials Technology and Engineering, Chinese Academy of Sciences, Ningbo 315201, China
[b] Center of Materials Science and Optoelectronics Engineering, University of Chinese Academy of Sciences, Beijing 100049, China

ARTICLE INFO

Article history:
Received 24 February 2025
Revised 8 June 2025
Accepted 8 June 2025
Available online 17 July 2025

Keywords:
Multilayer coatings
Mechanical properties
Multi-angle erosion
Foreign object impact
Failure mechanism

ABSTRACT

During low-altitude flight, take-off, and landing, aircraft compressor blades are vulnerable to significant erosion caused by airborne dust and sand particles propelled by high-speed airflow. In this study, Ti/TiAlN multilayer coatings with a gradient transition composite soft/hard alternating laminated structure were prepared on the surfaces of titanium alloys using arc ion plating technology. The mechanical properties and multi-angle resistance to foreign object damage of the coatings were evaluated in order to elucidate the deformation and strengthening mechanisms of the multilayer structure. The findings revealed that the coatings exhibited an adhesion strength exceeding 72 N, a hardness and elastic modulus of 25.1 GPa and 304.3 GPa, respectively. The impact depth of the coatings was reduced by over 20 % compared to the uncoated substrate. The enhanced resistance of the coatings to foreign object damage is primarily attributed to the hard TiAlN layer, which exhibits resistance to the cutting action of low-angle erosion particles. Concurrently, the soft Ti layer facilitates deformation at higher angles, promoting plastic deformation. Furthermore, the ceramic layer evidenced the decrease of stress concentration through mechanisms including grain refinement, transgranular microcrack propagation, and intergranular extension. The ductile layer served to enhance toughness by dissipating strain energy through mechanisms such as deformation twinning and dislocation generation.

1. Introduction

Particle erosion is defined as the process in which small, discrete solid particles impact a material surface at specific rates and angles, progressively removing materials from the surface [1–3]. In the context of turbine engines, compressor blades demonstrate a heightened vulnerability to structural damage at their tips, particularly when operating in challenging environments such as deserts. This heightened vulnerability is attributed to the erosion caused by solid particles. This erosion has a significantly adverse effect on the overall performance of the engine. The implementation of surface protective technology has been demonstrated to enhance the erosion resistance of titanium alloy blades, thereby extending their operational lifespan. It has been demonstrated that traditional low-temperature aluminized composite silicate coatings are inadequate in providing adequate protection in harsh environments. The resistance of the coating to erosion wear and foreign object impacts is closely tied to its hardness and toughness [4,5]. It has been demonstrated that high-hardness coatings are effective in mitigating plastic deformation that occurs under the impact of particles. In addition, high-toughness coatings have been shown to be highly efficacious in suppressing the propagation of cracks that are induced by such impacts [6–8]. The development of protective coatings that combine both high hardness and toughness on titanium alloy blades has the potential to offer significant benefits for a wide range of industrial applications.

Metal-ceramic multilayer structures exhibit a combination of high toughness and high strength, offering superior resistance to erosion damage [9–13]. Alan Zhang et al. demonstrated that the introduction of a TiAlN/TiAl multilayer structure via filtered cathodic vacuum arc technology significantly enhanced the toughness of monolayer TiAlN coatings [14]. The findings indicated that the hardness of the multilayer coatings decreased by only 15.46 %, while their erosion resistance was 1.9 times higher than that of the monolayer coatings under 90° high-angle sand erosion. The

---

[*] Corresponding authors.
E-mail addresses: wangzy@nimte.ac.cn (Z. Wang), aywang@nimte.ac.cn (A. Wang).

https://doi.org/10.1016/j.jmst.2025.06.029

combination of high hardness and toughness optimizes the erosion resistance of coatings. The erosion rate of coatings is influenced by several factors, including the angle of attack, the velocity of the particles, and the size of the particles. Bonu et al. deposited ultrathin multilayer coatings of Ti/TiN and TiAlN/TiN on Ti6AL4V substrates, which exhibited remarkable impact and corrosion resistance [15]. The erosion resistance of these coatings was evaluated at four distinct erosion angles: 90°, 60°, 45°, and 30°. The findings indicated that the TiAlN/TiN coatings demonstrated enhanced performance at reduced particle speeds. The enhanced erosion resistance of the coatings can be primarily attributed to the high density of interfaces, the multilayer architecture, and the incorporation of stress-absorbing layers. As demonstrated by Barshilia et al., deposited erosion-resistant ultrathin Ti/TiN multilayered coatings featuring porous and dense energy-absorbing Ti layers on Ti6Al4V substrates [15]. The findings of finite element simulations and experimental results demonstrated that at higher erodent speeds (50 to 100 m/s), porous Ti layers exhibited superior performance in comparison to dense Ti layer coatings. It is noteworthy that the corrosion resistance of the Ti/TiN-P coatings exhibited enhancement relative to the Ti/TiN-D coating as the erosion rate increased. In a similar vein, Bousser et al. investigated the influence of particle characteristics on erosion behavior [16]. The findings of the study indicated that multilayer structures exhibited a reduced propensity for damage from large, rounded particles. Erosion in multilayer coating systems was observed to occur in a layered manner when the particles eroded at a low speed.

TiAlN-based multilayer coatings have been identified as a promising solution for enhancing the erosion resistance of aero-engine compressor blades. However, the damage behavior and underlying mechanism of the coatings under multi-angle, variable-speed, and foreign object impact conditions remain largely unexplored. In our previous research, Ti/TiAlN multilayer coatings with varying deposition cycles (3, 6, 12, 24, and 72) were deposited on Ti-6Al-4V substrates using a multi-source cathodic arc ion plating system [17]. The erosion performance of these coatings was subsequently evaluated under silica sand and glass bead impact conditions [18]. In addition, the effect of incorporating different numbers of stress-absorbing layers (TiN-Ti-TiN) on the micro-nanomechanical behavior of the coatings and erosion resistance of the coatings was systematically investigated [19,20]. The failure behavior of the alternating soft/hard multilayer structure was analyzed in further detail, with the focus being on the role of the ductile metal layer in enhancing cracking resistance and understanding the microstructural evolution during deformation [21].

The present work elucidates the deposition of Ti/TiAlN multilayer coatings with a hard yet tough structure using multi-source arc ion plating equipment. The erosion rates of the coatings were evaluated at impact angles of 30°, 60°, and 90°, as well as under varying powder feed rates. The erosion damage behavior and mechanism of the coatings were further elucidated through an investigation of their micromechanical characteristics, surface damage morphology, and crack extension. This study provides a valuable reference for the multi-angle erosion protection of aero-engine blades and offers theoretical support for the design of new high-performance anti-erosion protective coatings.

2. Experiments

2.1. Coating deposition

Ti/TiAlN multilayer coatings were deposited on Ti-6Al-4V (TC4) substrates using a multi-source cathodic arc ion deposition system. This system was equipped with four independent arc ion sources and one linear ion beam (LIS) source. The LIS source was utilized for the plasma etching process, with the objective of achieving the complete removal of surface impurities. Ti targets (99.9 wt. % purity) were used for depositing both the Ti and TiN layers, while TiAl targets (Ti:Al atomic ratio of 33:67) were used for the TiAlN layer. All substrates (30 mm × 10 mm × 3 mm) were mechanically polished to a 5000-grit finish using SiC sandpaper, followed by ultrasonic cleaning in acetone and ethanol for 10 min each prior to deposition. In order to enhance adhesion strength, a Ti buffer layer was initially deposited onto the substrate surface under an Ar atmosphere. Subsequently, N_2 was introduced for the deposition of the TiN and TiAlN layers. During the deposition process, the base pressure of the chamber was maintained below 3×10^{-5} Pa, and the substrate temperature was controlled at 300 ± 5 °C. The jig was self-rotating and advanced sequentially in front of the different ion sources throughout the coating process. For a more comprehensive overview, please refer to our previous research. The resulting coating exhibited a Ti-TiN-TiAlN gradient transition structure and a Ti/TiAlN bi-periodic architecture, wherein the TiAlN hard layer imparted high strength, while the metal layer enhanced overall toughness. The TiAlN-based multilayer coatings exhibited optimal deformation coordination and comprehensive mechanical properties. The Ar/N_2 flux ratio was subject to intermittent adjustment during the deposition of the Ti and TiN layers, as outlined in Table 1.

2.2. Characterization methods

The surface and cross-section morphologies of the samples were observed using a scanning electron microscope (SEM, FEI Quanta FEG 250), while the chemical composition of the coatings was characterized by an energy dispersive spectrometer (EDS, OXFORD X-Max). The phase composition of the coatings was examined through the utilization of X-ray diffraction (XRD, Brucker D8 Advance) with Cu Kα radiation. Crystal-chemistry analysis of the as-deposited coatings was performed by X-ray photoelectron spectroscope (XPS, Kratos Axis ULTRA DLD) with Al Kα radiation. Furthermore, scratch tests (CSM Revetest, Switzerland) were conducted to evaluate the adhesion strength and crack extension resistance of the coatings. During testing, the indenter slid 5 mm across the coating surface at a speed of 2 mm/min, with the load progressively increased from 1 to 100 N. The preparation of cross-sectional samples commenced with preliminary cutting utilizing a low-speed saw (Buehler IsoMet$^{\text{TM}}$), subsequently followed by meticulous polishing employing an ion beam polisher (EM TIC 3X, Leica). Ion beam polishing, an ion bombardment-based technique, was employed to minimize deformation and strain in the polished region, thereby yielding high-quality cross-sectional specimens. The hardness and Young's modulus of the coatings were measured by a nano-indenter (G200, MTS) equipped with a Berkovich indenter. The fracture toughness of the coating surface was measured using a cube-corner diamond indenter (face angle $\varphi = 35.3°$). Ideal stresses and strains are generated in the contact area between the tip indenter and the coating, and fracture toughness can be evaluated through small-scale cracks around the indentation [20,22]. The indentation fracture toughness of the coatings was determined by using the equations as follows:

$$K_c = \alpha\left(\frac{E}{H}\right)^{1/2}\left(\frac{P}{c^{3/2}}\right) \tag{1}$$

$$\alpha = \frac{0.0352}{1-\nu}(\cos\varphi)^{2/3} \tag{2}$$

where P is the applied indentation load, E and H are the elastic modulus and hardness of the coatings, respectively. For a standard cube corner indenter, the value of α is an empirical constant depending on the geometry of the indenter, as illustrated in Eqs. (1) and (2) [23,24]. The crack lengths were derived directly

Table 1
Process parameters of cleaning and deposition.

Procedure	Flow (sccm)		Current (A)			Pressure (mTorr)	Substrate bias (V)	Time (min)
	Ar	N_2	Ion beam	Ti	TiAl			
Ion etching	35	0	0.2	–	–	1.5	−200	30
Buffer layer	200	0	–	70	–	45.0	−70	28
Transition layer	0	500	–	70	–	45.0	−70	80
Hard layer	0	500	–	–	80	55.0	−80	50
Soft layer	200	0	–	70	–	45.0	−70	3
Hard layer	0	500	–	–	80	55.0	−80	50

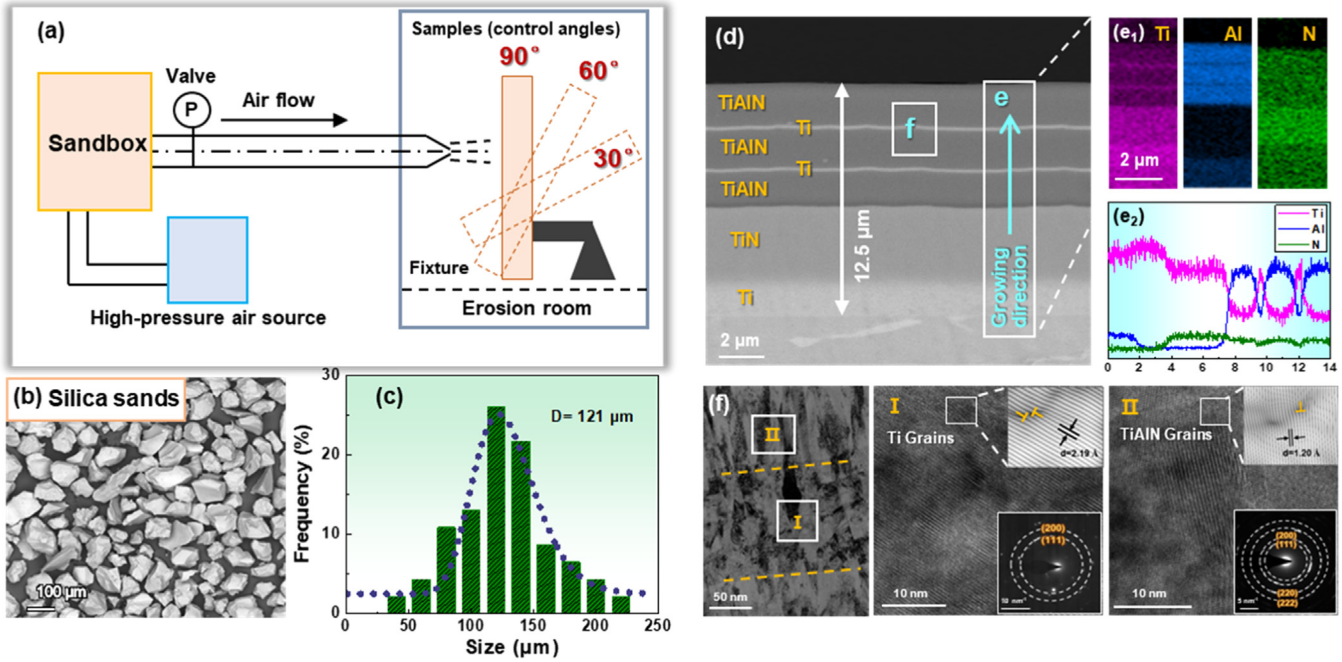

Fig. 1. (a) Schematic diagram of the erosion test, (b, c) morphology of silica erosion particles, (d) Ti/TiAlN multilayer coating structure, (e) cross-sectional EDS mappings, and (f) component characteristics of each sublayer.

from the SEM micrographs. Furthermore, Poisson's ratio v was set at 0.25 for the TiAlN-based composite coatings [25]. Furthermore, the conductive atomic force microscope (C-AFM) mode in a scanning probe microscope (SPM, Bruker) was used to obtain the surface morphology of the samples after nanoindentation. The microstructural evolution of the coatings was characterized using a transmission electron microscope (TEM, Talos F200x).

2.3. Foreign object damage test

The erosion test platform was designed in accordance with the standards for solid particle erosion testing as set out by the American Society for Testing and Materials (ASTM G76-18). As illustrated in Fig. 1(a), the erosion particles were delivered to a mixing chamber via a powder feeder, where they were combined with compressed air. This mixture was then accelerated through a nozzle and directed onto the coating surface. Compressed air served as the propulsion medium, enabling high-velocity particle impacts. The gas pressure was adjustable, allowing precise control over particle velocity and kinetic energy. Detailed descriptions of the apparatus can be found in our previous research [17]. The test parameters specified the use of polygonal quartz sand with a particle size of approximately 120–150 μm as the erosion medium. The speed of the particles (0–120 m/s) was modulated through the regulation of the air pressure within the feed bin. The erosion rate, which indicates the coating's resistance to erosion, was determined using the weight loss method. The change in mass of the samples during the erosion test was measured with an analytical balance that has a resolution of 0.01 mg (Mettler Toledo, XS205 DU). The erosion rate of the coatings was calculated by the weight loss method as shown in Eq. (3). Each sample was subjected to at least three tests. Before and after testing, the samples were cleaned with absolute ethanol for 10 min and then dried.

$$\text{Erosion rate}\,(\text{ER}) = \frac{\text{Mass of specimen removed (mg)}}{\text{Mass of impacting particles (g)}} \tag{3}$$

During take-off, landing, or low-altitude flight, engine components (primarily fan or compressor blades) are susceptible to impacts from foreign objects ingested by high-speed airflow. The damage caused by the impact of foreign objects, such as metal pieces, stones, or sand particles, is referred to as "foreign object damage" or "foreign object impact" [26]. The foreign impact test was conducted using air cannon systems [27]. The operational principle of the air cannon entailed the expansion of compressed air, thereby accelerating the bullet holder (including foreign objects) and inducing their ejection from the barrel. A speed measuring device was positioned at the rear of the barrel to quantify the velocity of foreign objects. The bullet holder and the foreign object were ejected at a certain speed for a certain distance, and then collided with the bullet holder separator, resulting in the separation of the bullet holder and the simulated foreign object. The foreign object subsequently continued to travel a certain distance before impacting the target. The velocity of the foreign object could be modulated by adjusting the pressure of the compressed air. The kinetic energy during foreign object impact on the sample surface was determined by Eq. (4), in which m denotes the impactor's mass and v (its velocity). It is important to note that, in order to avoid impactor disintegration and to ensure higher-energy impacts, the size parameters (such as diameter or edge length) of the foreign object were carefully optimized. In the present study, glass beads of varying diameters were utilized to establish distinct impact conditions. Beads with a diameter of 2.5 mm generated low-velocity impacts at 250 m/s, while larger beads (3 mm in diameter) produced high-velocity impacts at 350 m/s.

$$E = \frac{1}{2}mv^2 \tag{4}$$

$$m = \frac{4}{3}\pi r^3 \rho \tag{5}$$

2.4. Micropillar compression test

Micropillars with a diameter of 1.2 μm and a height of 3.6 μm were fabricated using a dual-beam focused ion beam (Helios-G4-CX) at an accelerating voltage of 30 keV. The aspect ratio was maintained below 3:1 to prevent bending or flexing during compression [27,28]. The micropillars under consideration consisted solely of TiAlN sublayers and a thin Ti layer. The configuration under consideration was employed to facilitate compression testing of the Ti/TiAlN multilayer micropillars. This enabled systematic testing and analysis of failure behavior at the Ti-TiAlN interface. All micropillars were fabricated using an annulus milling technique [29]. Initially, a beam current of 9.3 nA was employed for coarse milling to form the columns, which were subsequently refined using a beam current of 1 nA. Final polishing was performed with a beam current of 80 pA to minimize surface damage. Uniaxial compression testing was performed using a Bruker TI 980 Triboindenter equipped with a flat-punch diamond indenter. At least three micropillars of each type were tested under displacement-controlled loading. Engineering stress and strain were calculated using $\sigma = F/A_0$ *and* $\varepsilon = \Delta h/h_0$, where F is the applied force, A_0 is the initial cross-sectional area, Δh is the change in height, and h_0 is the initial height [30]. To characterize the deformation mechanism, plate-like samples containing micropillars were thinned to electron transparency for further TEM characterization.

3. Results and discussion

3.1. Microstructure characterization

As illustrated in Fig. 1(a), erosion particles were propelled by compressed air to impact the sample surface. By modifying the sample angle, a range of multi-angle erosion scenarios was simulated. The particle size distribution of erosion particles is shown in Fig. 1(b) and (c), with the average particle size of polygonal quartz sand measured at 121 µm. Samples produced by vacuum arc deposition have been shown to exhibit higher deposition efficiency, strong bond strength, and excellent mechanical properties. The benefits are attributable to the elevated degree of ionization, the substantial ion energy, and the considerable plasma generation rate in the cathode spot [31]. Fig. 1(d) displays the coating structures and cross-sectional morphologies of the as-deposited coatings, which maintain a total thickness of approximately 12.5 μm. The Ti bottom layer and TiN load-bearing layer have a thickness of about 2.0 and 4.0 μm, respectively. The alternating soft and hard Ti/TiAlN periodic structure maintains an optimal thickness ratio of 1:20, with the Ti soft layer measuring 100 nm and the TiAlN hard layer 2 μm thick. The role of the Ti bottom layer is to enhance adhesion between the substrate and the coating, while the thick TiN transition layer provides load-bearing capacity and creates a mechanical property gradient between the Ti and TiAlN layers. The introduction of extremely thin Ti ductile layers serves to absorb impact energy, with stress-relief zones strategically positioned between the TiAlN hard layers. The TiAlN layers exhibit superior erosion resistance, attributable to their mechanical properties [18]. The EDS results (Fig. 1(e)) show distinct interfaces between the sublayers in the multilayer structure and significant composition contrast. Line scan analysis of the cross-section further demonstrates the typical periodic distribution of each element. High-resolution TEM (HRTEM), selected area electron diffraction (SAED), and fast Fourier transform results in Fig. 1(f) confirm that the multilayer interfaces exhibit a stable phase structure, with the Ti and TiAlN sublayers displaying characteristic crystal structure properties. These findings were consistent with the XRD results shown in Fig. S1 in the Supplementary Materials and the XPS analysis presented in Fig. S2.

3.2. Mechanical properties

The adhesion strength of multilayer coatings was evaluated using a progressive micron scratch test, as shown in Fig. S3. The results indicate that the coatings exhibit an adhesion strength of up to 72 N [32,33]. At the critical load of L_{c3}, surface morphologies reveal buckle spallation failure modes accompanied by river-like cracks, which are characteristic of hard coating scratching on soft substrates, driven by tensile stress and friction [34,35].

The hardness and Young's modulus of the multilayer coatings were evaluated using the continuous stiffness method with a Berkovich indenter. To minimize substrate influence, the indentation depth was restricted to no more than one-tenth of the total coating thickness [36]. Fig. S4(a) presents the load-displacement curves obtained during nanoindentation, demonstrating elastic recovery of up to 43 %. The hardness and modulus decrease with increasing indentation depth, stabilizing at approximately 10 % of the coating thickness, as shown in Fig. S4(b). This behavior is attributed to the alternating soft and hard layers in the multilayer structure. At 10 % depth, as shown in Fig. 2(a), the hardness and elastic modulus were measured at 25.1 ± 2.3 GPa and 304.3 ± 0.7 GPa, respectively. The H^3/E^2 ratio, which is a measure of the material's resistance to the onset of plastic deformation, and the H/E ratio are significant in the case of abrasive or erosive wear [16,37]. The parameters $H^3/E^2 = 0.171$ and $H/E = 0.082$ indicate the superior elastic-plastic deformation and abrasive wear performance.

Fracture toughness was assessed using sharp cube corner indenters, which significantly reduced the indentation-cracking threshold, enabling measurement at minimal loading forces [38,39]. Cube corner nanoindentation testing was performed at 300, 400, and 500 mN, as shown in Fig. S5. Under a 300 mN load, the coating exhibits no significant radial crack extension at the indentation tip. At 400 mN, radial cracks are observed at the indentation tip, along with noticeable plasticity build-up. This plasticity facilitates stress relaxation and absorbs substantial strain energy, limiting radial crack propagation. At 500 mN, however, radial cracks extend significantly, accompanied by signs of coating chipping, typical of local stress release. The appropriate crack lengths observed in the nanoindentation surface topography provide the basis for fracture toughness calculations. The calculation process of fracture toughness is demonstrated in Tables S2 and S3. The fracture toughness of the Ti/TiAlN multilayer coating was analyzed when significant cracks were present at 500 mN, and the value was found to be 6.72 MPa $\text{m}^{1/2}$. It is important to note that the crack length at the indentation tip exerts a significant influence on

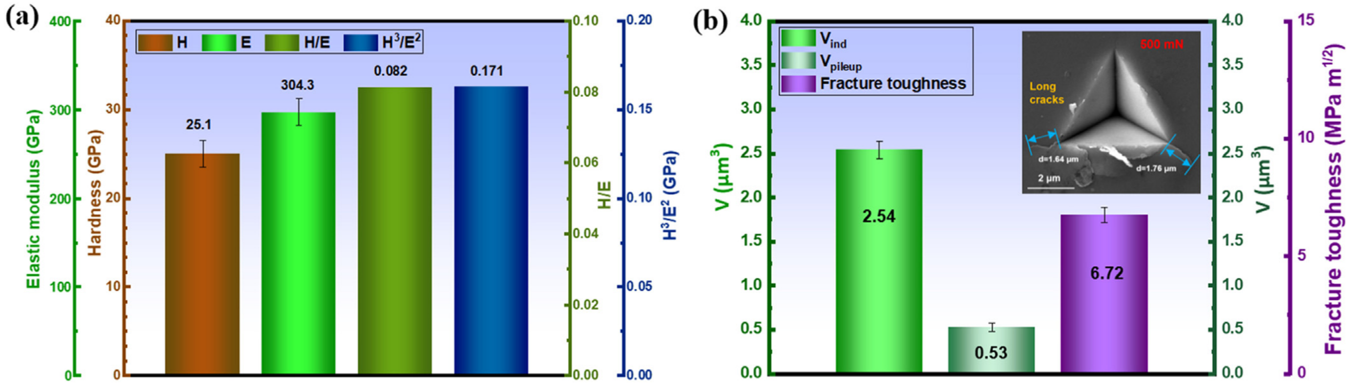

Fig. 2. (a) Micro-mechanical properties of Ti/TiAlN multilayer coatings at a depth of 10 %, (b) surface morphology and fracture toughness of coatings after 500 mN indentation.

the fracture toughness. As demonstrated in Table S2, the toughness value at 400 mN without significant long crack formation exceeds 11 GPa. The enhanced potential of toughness can also be attributed to the effective stress buffering of the ductile layers and the optimal Ti-TiN-TiAlN gradient transition in the multicycle structures. The aforementioned properties contribute to the coatings' enhanced toughness and resistance to cracking, thereby reflecting the "hard yet tough" nature of the coatings.

As illustrated in Fig. S6, the AFM topography maps and the corresponding cross-section profiles of the indentations on the Ti/TiAlN coatings are presented. The term 'V_{ind}' is employed to denote the total material volume that is displaced by the indenter. The term 'V_{pileup}' is used to denote the volume of plastically deformed material that is extruded upward around the indentation. The indentation volume and pile-up volume were obtained according to the height profile integral measured by AFM. As demonstrated in Fig. S6(c) and (d), the ratio of $V_{\mathrm{pileup}}/V_{\mathrm{ind}}$ (20.8 %) exhibits a comparable result to the elastic response (25.5 %) of TiAlN coatings under a 500 mN cube-corner indenter. The low $V_{\mathrm{pileup}}/V_{\mathrm{ind}}$ ratio is indicative of brittle fracture and high strain hardening capacity.

3.3. Multi-angle erosion behavior

3.3.1. Different feeding amounts of powder

The long-term protective efficacy of the coating was assessed through continuous erosion testing conducted at multiple angles [40]. The powder feed speed was controlled by adjusting the duration of the erosion process, with a typical feed rate of approximately 2 g/min. The erosion pressure was set at 0.2 MPa, and the particle speed was approximately 40 m/s. Fig. 3 illustrates the effects of different powder feeding amounts on the erosion rate of both the coating samples and the substrate across all angles. Initially, the uncoated sample exhibits a higher erosion rate, especially at the start of the erosion process (with 5 g of powder). As the erosion progresses, the rate fluctuates slightly before stabilizing at an equilibrium value of approximately 0.1 mg/g. For coated samples, the erosion rate gradually increases over time. When the powder feeding amount reaches around 30 g, the erosion rate at all angles tends towards stability, with the lowest rate observed at higher angles of attack. This contrasts with the higher erosion rate observed at large angles of attack before 15 g of powder, where the protective efficacy of the coatings appears to diminish due to damage and breakage. As the erosion process continues, the coating becomes progressively damaged, exposing the underlying matrix. This shift results in the characteristic erosion behavior of ductile materials, marked by increased tolerance to high-angle erosion compared to low-angle cutting. It is evident that, in the course of the long-term erosion process leading to peeling, the erosion rate of the coating is consistently below 0.1 mg/g. This represents a substantial enhancement when compared with the conventional single-layer structure and with the results previously published [19].

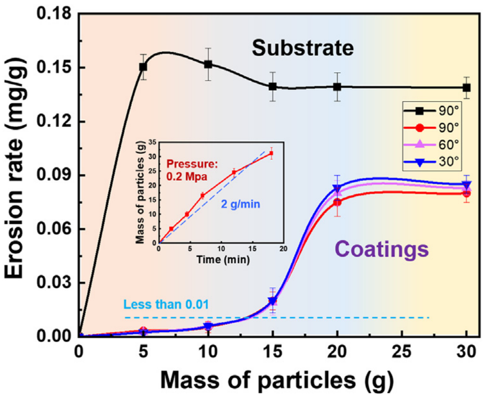

Fig. 3. Erosion rate of Ti/TiAlN multilayer coatings under different powder feeding amounts.

Fig. 4(a) and (b) illustrates the 3D contour morphologies of the coatings and substrate following high-angle (90-degree) erosion by particles of varying masses. All samples exhibit varying degrees of surface damage. Prior to the erosion of particles with a mass <15 g, the coatings exhibit minimal surface damage, with only minor pitting observed. Some pitting extends downward, but no large-scale peeling occurs. At a powder feeding mass of 20 g, the damage area on the coating surface expands significantly, with the maximum erosion depth penetrating the coating, resulting in its complete removal. This observation is further supported by the detailed surface profile in Fig. S7. In contrast, the uncoated samples (Fig. 4(b)) exhibit greater initial damage, with the affected area continuing to expand as the erosion process progresses.

Fig. 4(c) and (d) presents the statistical results of the damage depth and area after erosion. As the quantity of erosion powder increases, both the damage depth and area of the matrix material show a linear increase. However, the TiAlN coatings exhibit strong protective efficacy, with both erosion depth and damage area reduced by more than one order of magnitude compared to the substrate until the erosion particle mass reached its limit. As the erosion process continues, numerous pitting sites rapidly form and converge on the coating surface, ultimately resulting in the development of a crater structure. The damage depth of the coating increases significantly from 9.3 to 137.1 μm when the erosion particles reach 20 g, indicating that the protective effect is substan-

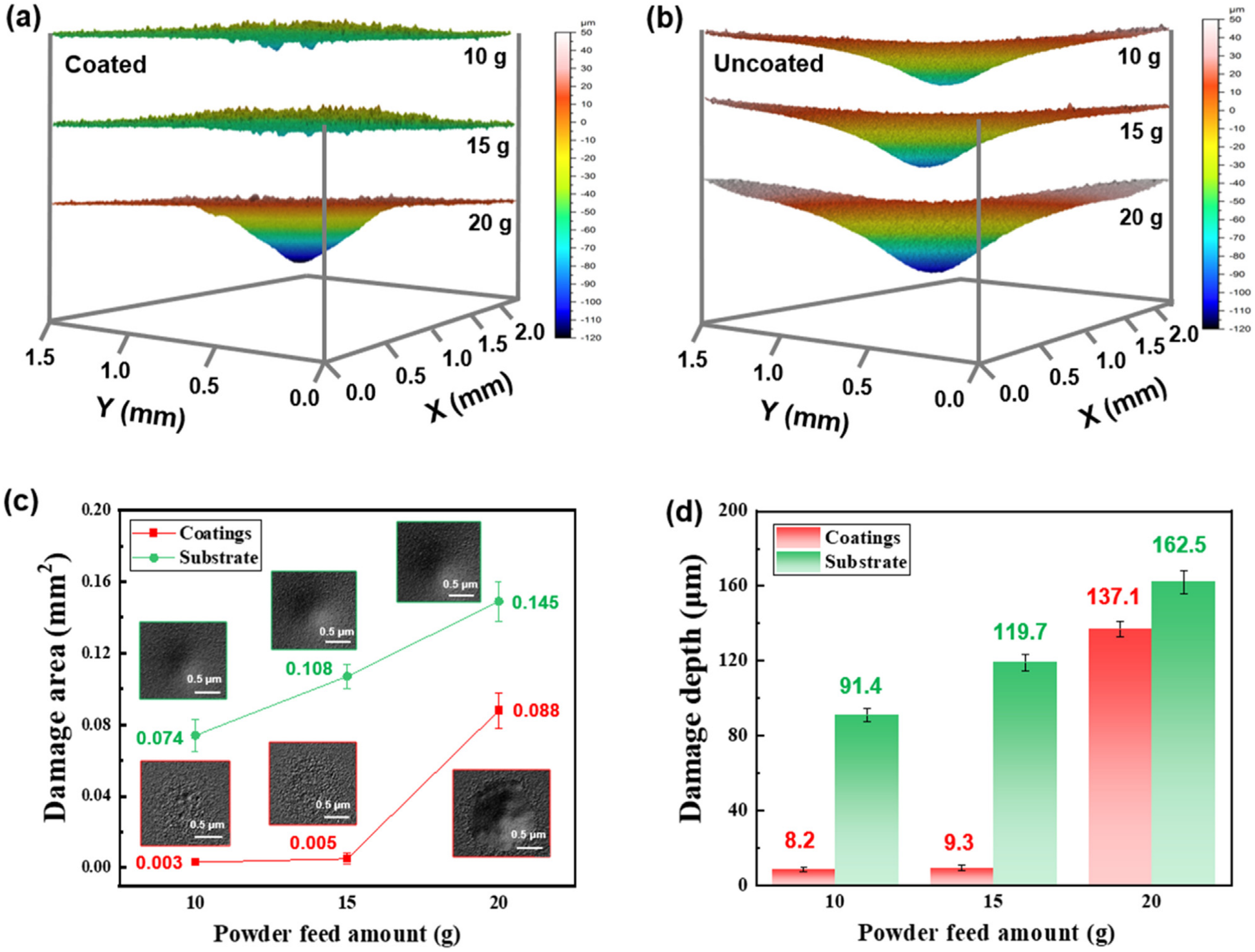

Fig. 4. (a, b) Surface 3D contour morphologies of the coatings and substrate at 10, 15, and 20 g of erosion particle amounts, (c, d) damage depth and area reflected by the erosion pits on the sample surfaces under different erosion conditions.

tially diminished after coating failure. The hard yet tough Ti/TiAlN multilayer structure proves crucial in protecting the substrate from erosion damage.

3.3.2. Different erosion speed of particles

The primary factors influencing sand and dust erosion rate are the quantity of sand supplied and the particle speed. Subsequently, a series of tests were conducted under varying particle velocities during the stable erosion stage (after 10 g of powder). The erosion rates of samples that had been coated and uncoated with Ti/TiAlN multilayer coatings were evaluated in Fig. 5. The speed of the particles was modulated by means of a control system that adjusted the air pressure within the feed bin. The findings indicate that, under both high-speed (80 m/s) and low-speed (40 m/s) erosion conditions, the erosion rates of the coating samples remain consistently around 0.01 mg/g. This is approximately one order of magnitude lower than that of the substrate. In the case of 40 m/s of erosion conditions, the Ti/TiAlN coating exhibits its minimum erosion rate of 0.004 mg/g at a 30° impact angle, while the maximum rate of 0.006 mg/g is recorded at 90°. Conversely, under 80 m/s erosion conditions, an inverse trend was observed: the coating exhibits peak erosion rate (0.016 mg/g) at 30° impact angle, with the lowest rate (0.013 mg/g) recorded at 90°. This opposing trend is consistent with the evolution of the erosion rate under continuous erosion depicted in Fig. 3. This is due to the fact that, at low speeds or low particle density, the damage to the coating surface is limited, and the hard and brittle TiAlN top layer provides the sample with good strength to resist scouring wear. However, it has been demonstrated that continuous scouring or higher-energy particle impacts accelerate fatigue damage and even spalling of the top layer [41]. This renders the influence of the ductile layer and substrate on the coating performance more significant [42]. Consequently, the coating manifests properties more akin to a ductile material, thereby enhancing its resistance to high-angle impacts.

For the uncoated substrate, both high-speed and low-speed erosion demonstrate a trend where the erosion rate decreases with increasing angle of attack. As a ductile material, the substrate mitigates stress concentration through plastic deformation during vertical impact, resulting in a relatively low erosion rate. At low angles of attack, material removal occurs in larger pieces due to the plowing effect, which leads to a higher erosion rate. In contrast, for the coated samples, surface strengthening enhances the mechanical properties of the materials. Consequently, under low-angle erosion, the increased hardness of the coating provides superior resistance to micro-cutting, resulting in minimal weight loss. However, high hardness often correlates with brittleness, and under a 90-degree impact angle, the coating is susceptible to brittle peeling, which significantly raises the erosion rate. Overall, the coated sample demonstrates a more effective protective capability across all angles under both high-speed and low-speed erosion conditions.

As shown in Fig. 6, the surface damage morphologies of the coating after erosion at different particle velocities are presented. Under low-speed vertical erosion (Fig. 6(a)), the hard and brittle nature of the coating material leads to the formation of numerous

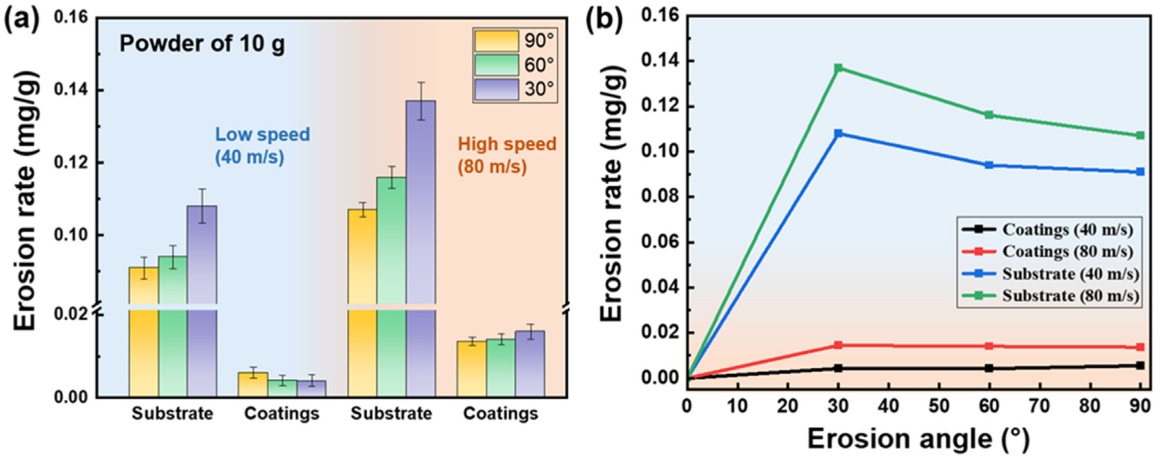

Fig. 5. Erosion results of Ti/TiAlN multilayer coatings at (a) different particle speeds and (b) multi-angle erosion conditions.

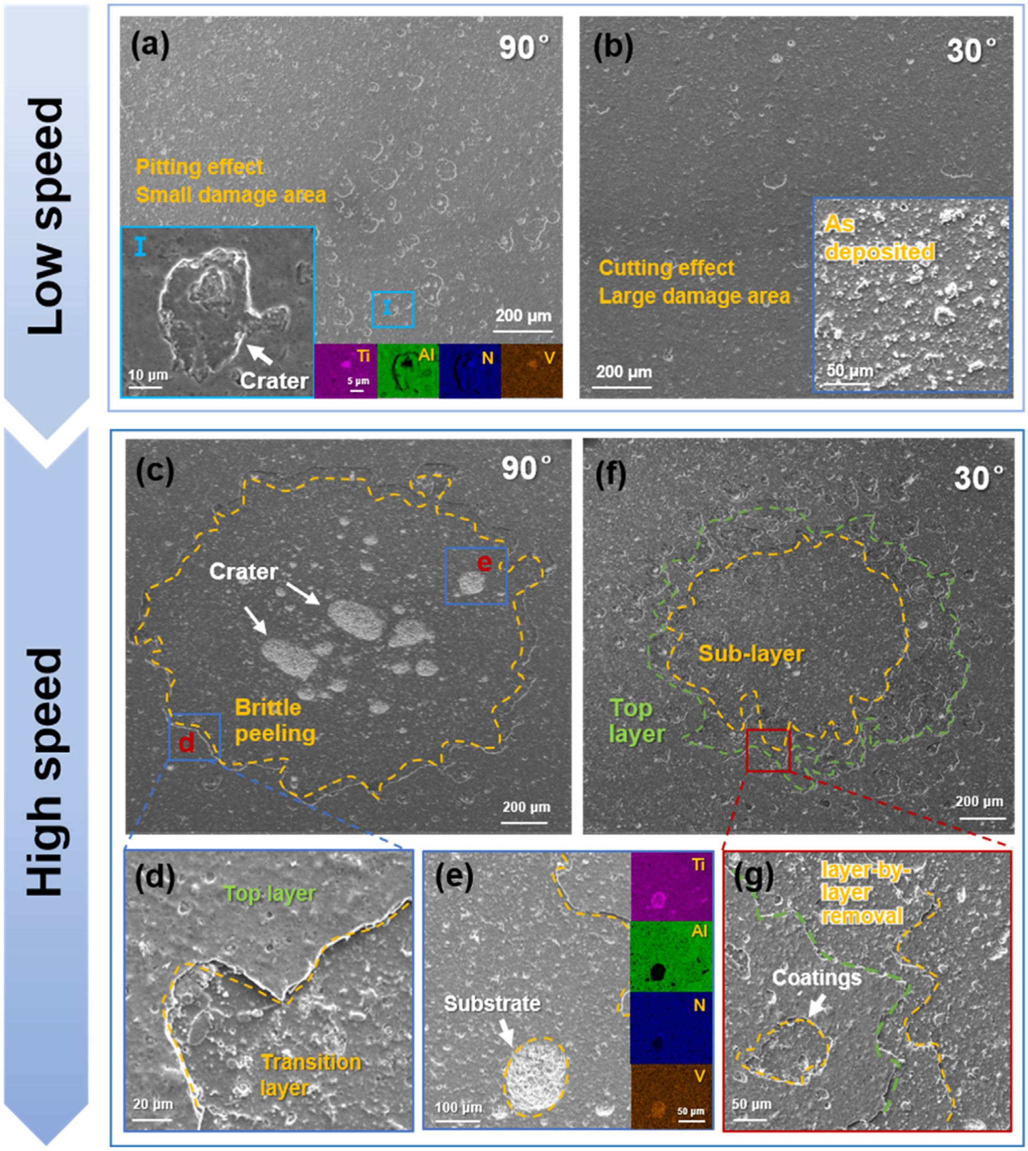

Fig. 6. Surface morphologies of the samples after erosion test at (a, b) low speed and (c–g) high speed.

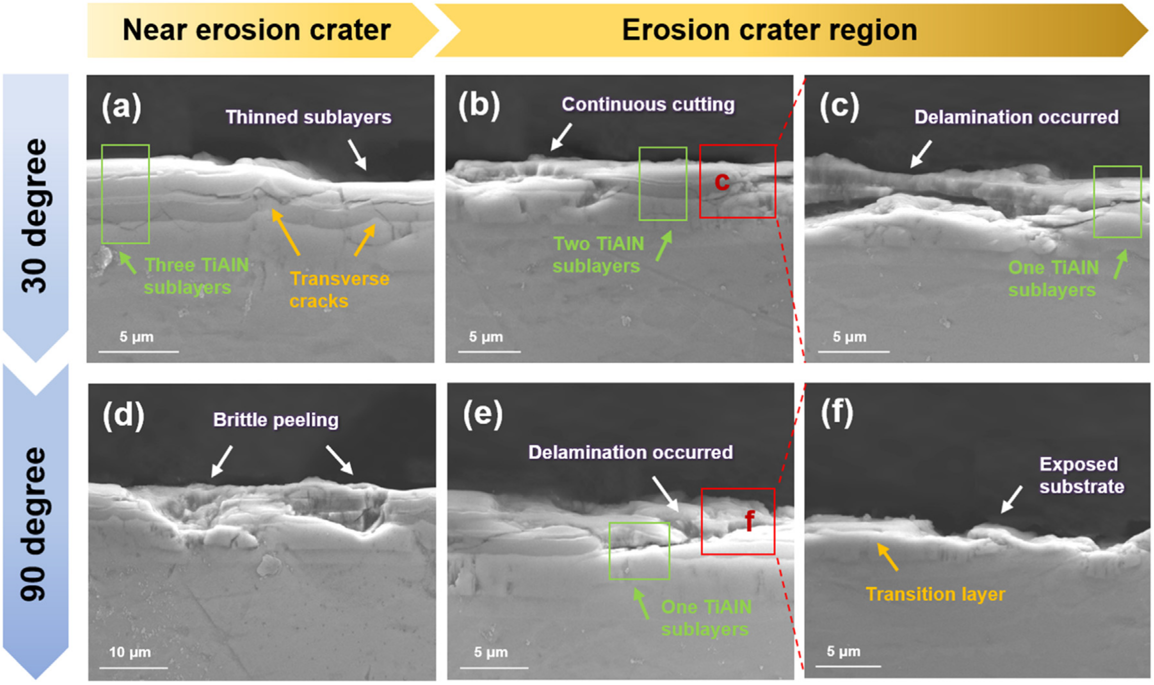

Fig. 7. Cross-sectional morphologies of the samples after erosion test at (a–c) 30° and (d–f) 90°.

erosion pits emerging on the surface. Magnified images reveal that the pits have penetrated the substrate but have not yet interconnected to trigger large-area brittle spalling. Low-speed erosion at a 30-degree angle (Fig. 6(b)) is dominated by micro-cutting, where large particles are removed from the coating surface under a “polishing” effect. The surface damage of the coating is significantly exacerbated under conditions of high-speed erosion (Fig. 6(c) and (d)). At a 90-degree erosion angle, a large circular damage area emerges, characterized by multiple erosion pits that fully penetrate the substrate. A close-up view of the damage (Fig. 6(e)) reveals that the edge of the damaged region exhibits a layered, fractured TiAlN sub-layer structure. In the central region, where severe erosion occurs, the coating is completely removed, exposing the underlying substrate within the erosion pit and compromising its protective function. In contrast, during low-angle erosion (Fig. 6(f) and (g)), the damage area is significantly reduced. The edge of the damaged region exhibits a layer-by-layer removal phenomenon, with no evidence of penetrating erosion pits. This observation supports the conclusion that low-angle erosion results in a lower erosion rate. In addition, high-speed erosion induces a characteristic failure mechanism in the coating, with material removal occurring primarily by crushing deformation. It has been demonstrated that high-speed erosion has the capacity to induce a fracture within the coating. The removal of materials occurs under the action of “microcrack-driven” and “cyclic damage” accumulation. In contrast, oblique scouring leads to a combination of micro-cutting and deformation, manifesting as a layer-by-layer flaking mechanism.

As demonstrated in Fig. 7, the cross-sectional morphology following high-speed erosion at high/low angles of attack is evident. Fig. 7(a–c) illustrates the morphological characteristics in the vicinity of the erosion pit and within the pit area itself. It is evident that during low-angle erosion, the multi-layer structure undergoes a process of gradual thinning, accompanied by the formation of a substantial number of transverse cracks. These transverse cracks are a consequence of the action of micro-cutting. As the erosion center is approached, the damage intensifies, and the coating continues to be cut and thinned. This process is accompanied by the extension and propagation of transverse cracks at the interface until the complete delamination and spalling of the TiAlN sublayer, exposing the substrate. As demonstrated in Fig. 7(d–f), the failure process of high-angle erosion is evident, thereby demonstrating that vertical impact initially induces brittle spalling of the contacted material, resulting in through-type damage. As the erosion effect intensifies, the coating gradually fractures and is removed. This process is accompanied by the fragmentation and removal of the entire TiAlN multilayer structure. The underlying mechanism is the stress concentration effect in the impact zone, which exacerbates the downward propagation of radial cracks, leading to the overall delamination of the coating.

3.4. Resistance to foreign object impact

A high-energy particle impact test was conducted to characterize the coating’s resistance to damage from foreign objects under harsh conditions [41,43]. Fig. 8 shows the crater morphologies and the damage effects on both the substrate and coatings following a vertical impact test. The low-speed impact test employed glass beads with a diameter of 2 mm and an impact rate of 250 m/s, while the high-speed impact test used glass beads with a diameter of 3 mm and an impact rate of 350 m/s. It is evident that all samples experience a significant impact, resulting in the formation of distinct craters. As the impact velocity increases, both the area and depth of damage grow substantially. As demonstrated in Fig. 8(a), the damage depth of the coating sample is reduced by 22.8 % compared to the base material under low-speed impact. Following the deposition of the protective coating, the damage depth of the sample is reduced by 20.9 % under high-speed impact. The Ti/TiAlN multilayer coatings significantly improve the material’s resistance to foreign object damage.

Fig. 9 illustrates the morphology and structural characteristics of the TiAlN coating following high-speed impact. As shown in Fig. 9(a), the damaged region resulting from the impact event exhibits a circular morphology with a diameter of 1.1 mm. Upon a high-energy foreign object, the coating cracks and adheres to the surface of the softer substrate under the compressive force of the

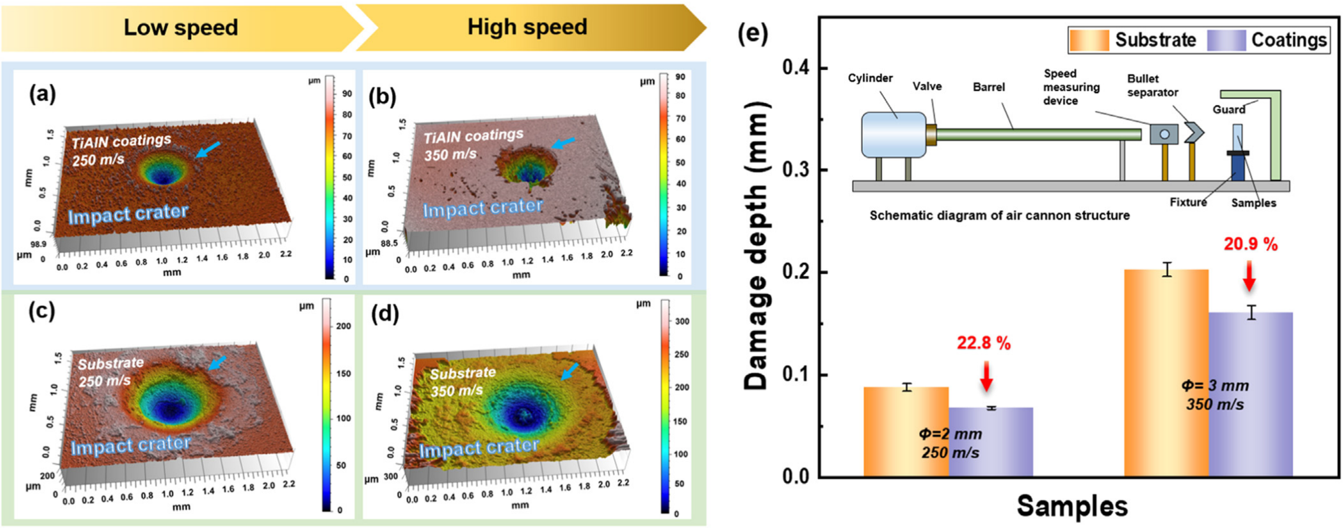

Fig. 8. Crate morphologies of substrate and coatings after impact of glass beads at (a, c) 250 m/s and (b, d) 350 m/s, (e) impact resistance of the samples reflected by the damage depth.

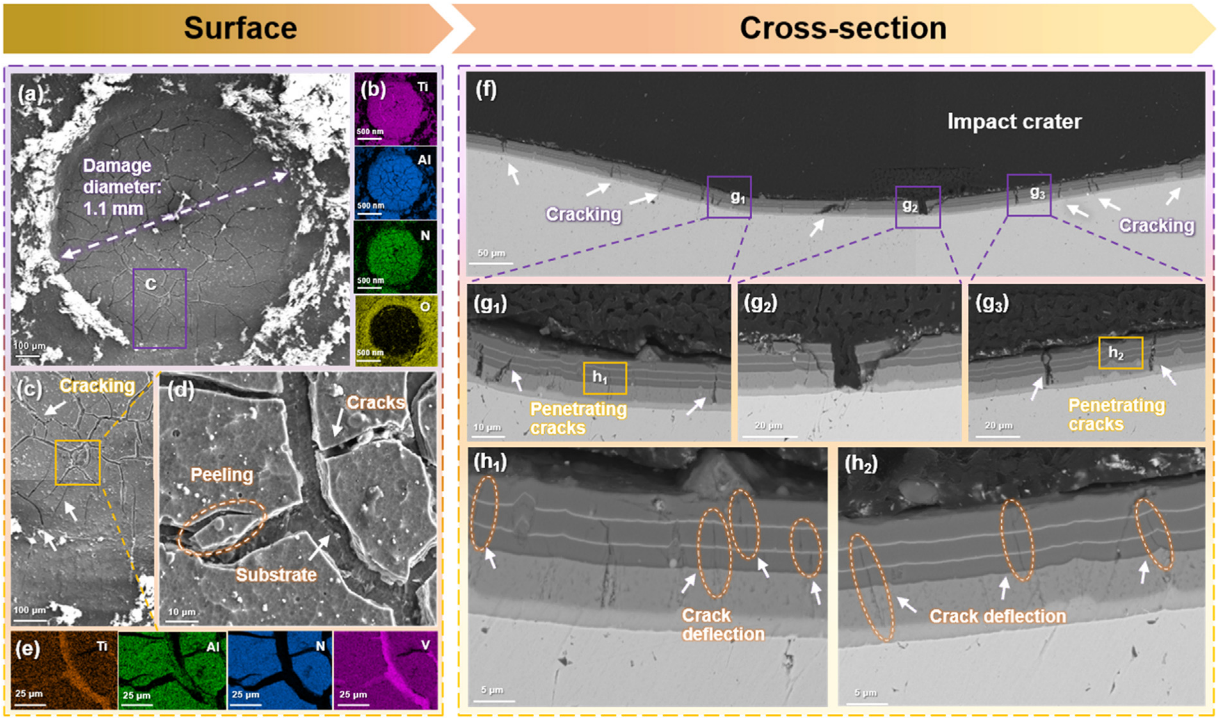

Fig. 9. (a) Surface morphologies and (b) EDS characteristics of the crater after high-speed impact, (c) fragmentation coatings and (d, e) enlarged cracking details; (f) cross section morphologies of the damage center, significant (g) penetrating cracks and (h) deflection cracks.

foreign object. EDS results of the damaged region (Fig. 9(a)) show that the coating does not detach from the substrate. The observed enrichment of oxygen around the erosion pit can be attributed to the sputtering of alumina glass beads upon impact with the coating surface. Fig. 9(c) provides a magnified view of the damaged area. Due to the inferior plastic deformation ability of the hard coating compared to the substrate, the cracks become more severe towards the center of the impact site. EDS analysis of the broken area (Fig. 9(e)) reveals a significant enrichment of vanadium (V) within the crack, indicating that the crack has penetrated into the substrate.

Fig. 9(f–h) illustrates the cross-sectional morphology of the damage center following high-speed impact. As seen in Fig. 9(g_2), large, deep penetrating cracks are present at the center of the coating, the area most severely deformed by the impact. Further from the center, the cracks gradually narrow (Fig. 9(g_1–g_3)), with some extending to the coating surface. Fig. 9(h_1) and (h_2) shows the propagation of microcracks within the coating. In the context of an impact test, the substrate alloy and the coatings exhibit a phenomenon of co-deformation. The microcracks primarily originate from the TiN layer at the bottom and then propagate upward due to the good bond strength between the transition layer and the metal substrate in the multilayer structure. When the crack passes through the stress-absorbed Ti layer, it usually twists and bends. The existence of the stress-absorbing structure thus plays a role in restraining crack propagation.

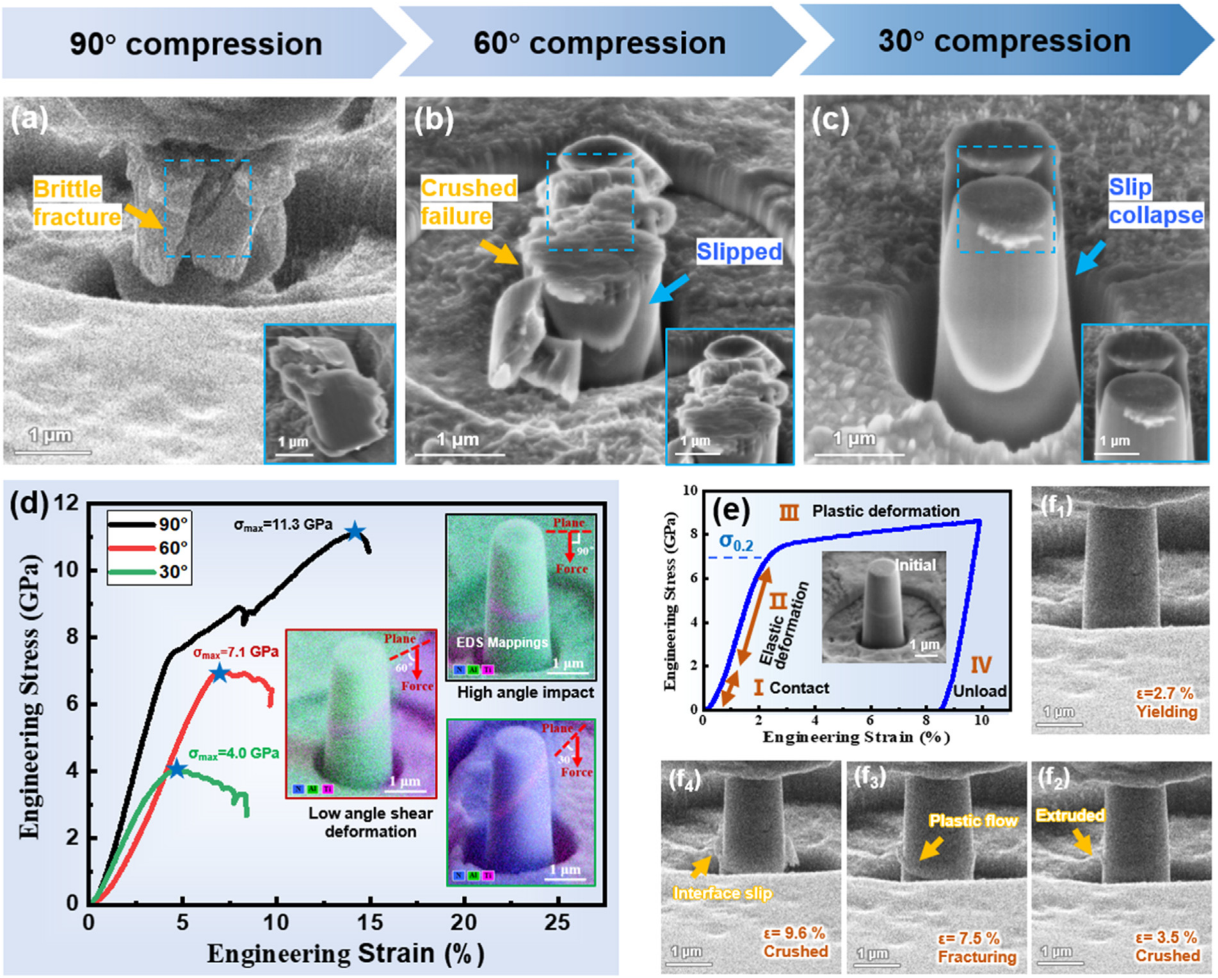

Fig. 10. Interfacial shear failure behavior of micropillars with different sublayer inclination angles after compression: (a) 90° compression, (b) 60° compression, (c) 30° compression, (d) engineering stress-strain curves; (e, f) characteristic evolution during in situ compression.

3.5. *Deformation mechanism*

3.5.1. *Interfacial shear failure behavior*

The shear deformation behavior in different directions of multilayer coatings was evaluated through in situ micropillar compression tests. Despite the marked difference in scale between micropillar compression tests (micrometer-level) and actual components (millimeter-level), these tests remain effective in revealing material degradation behaviors, particularly with regard to deformation mechanisms. The evolution of mechanical behaviors, such as interface failure, is minimally affected by size effects due to the micropillar dimensions (3.6 μm) significantly exceeding the material's characteristic length scale (mean free path of dislocations $\approx$ 100 nm). This ensures that plastic deformation is governed by the same fundamental mechanisms (dislocation slip and grain boundary interactions) as in macroscopic specimens. Furthermore, the failure mechanisms at the interface are predominantly influenced by interfacial bonding strength (a scale-independent parameter) and stress gradients. Pre-tilted interfaces were fabricated within the micropillars. The objective of this study was to facilitate the characterization of interfacial stress states and failure modes under shear deformation. This process effectively simulates the mechanical responses to oblique impact conditions.

Fig. S8 illustrates the machining diagram of micropillars with varying layer-oriented structures. Figs. 10(a–c) and S9 depict the morphology of the micropillars after compression failure, with compression directions of 90°, 60°, and 30° depicted. Fig. 10(d) presents the load-displacement curves during the compression process of micropillars with different layer orientations, along with the corresponding original EDS mappings of the micropillar structure. The compression directions were defined by the angle between the load direction and the multilayer interface orientation during uniaxial compression. It is evident that, during vertical compression, significant brittle fracture occurs within the microcolumn, particularly damaging the TiAlN sublayer on the uppermost surface. The 60-degree sample shows similar brittle fracture, accompanied by slippage of the ceramic layer along the interface. For the 30-degree sample, the primary failure mode is dominated by interface slip, with the hard layer collapsing downward along the interface. This occurs because the metal layer, having relatively low yield strength, allows plastic flow, which further promotes interface slip failure. During low-angle compression, the shear component along the interface is maximum, making it easier to reach the shear strength limit of the interface, which ultimately leads to interface delamination.

As shown in Fig. 10(d), as the compression directions decrease, both the strain at coating fracture and the ultimate compressive strength gradually decrease. This reduction is due to the increased likelihood of slip along the interface direction when the multilayer structure is deformed due to the pre-set inclination angle. Consequently, micropillars with high interface inclination angles are more prone to inducing slip deformation and early-stage stress release. The 90-degree micropillars achieve a maximum compressive strength of 11.3 GPa at a deformation of 14.1 %, while the

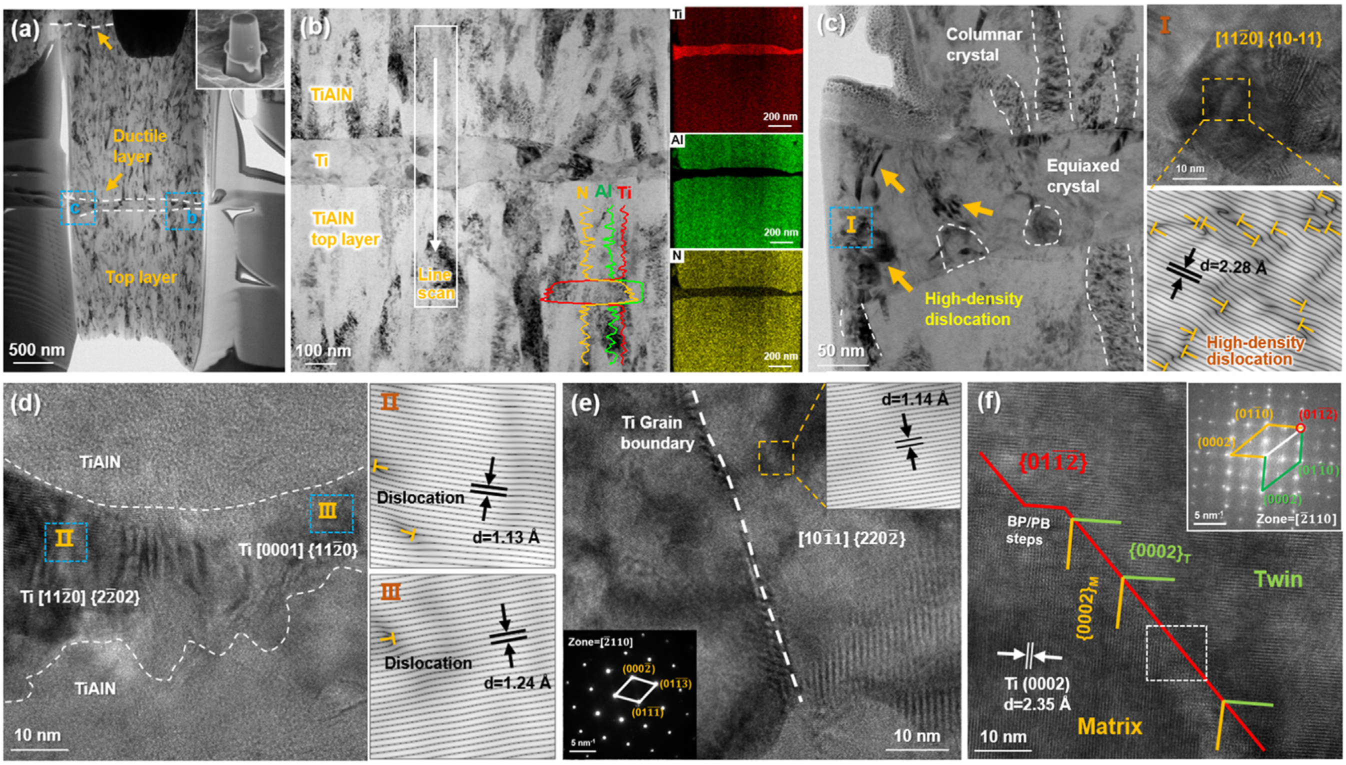

Fig. 11. Microstructure evolution of Ti/TiAlN multilayer coatings after compression: (a) internal structure information of the compressed sample along the axis cross-section direction, (b) morphology and EDS results of the multilayer structure, (c) plastic extrusion accompanied by high-density dislocations in ductile layer, (d) HRTEM image of Ti-TiAlN interface, (e) HRTEM image of Ti grains with nearly parallel crystal zone axes, and (f) deformation twins in the ductile layer.

60-degree and 30-degree micropillars reach ultimate compressive strengths of 7.1 and 4.0 GPa, respectively. Notably, the 90-degree sample exhibits a sudden stress drop at approximately 7.9 % deformation, after which the strengthening effect resumes. At this point, significant plastic extrusion occurs in the ductile layer. In the absence of a predefined slip surface, continued compression leads to stress concentration in the top layer, ultimately causing failure. The interface shear deformation behavior aligns with the characteristics observed in multi-angle erosion failure. Specifically, fatigue cracking occurs due to stress concentration at high angles, while the low-angle cutting effect weakens the interface bond. Energy is primarily absorbed through interface slippage and delamination, leading to overall collapse and layer-by-layer peeling.

Additionally, by actively unloading the force after a period of deformation, the deformation details of the multilayer structure under small strains were captured. Fig. 10(e) and (f) shows the load-displacement curve and deformation process of the sample before crushing. The point at which plastic deformation reaches 0.2 % is typically defined as the yield point. It is observed that the sample yields at a deformation of 2.7 %, though no significant plastic flow occurs at this stage. The micropillars then undergo continuous work hardening, with stress increasing in tandem with plastic deformation. During the crushing process, the soft layer experiences some plastic extrusion, while the hard layer remains largely intact, a characteristic behavior of multi-layered systems under compression [44,45]. Ultimately, when the strain reaches 9.6 %, the tough layer within the micropillar is almost completely extruded. If the stress continues to rise, localized interface sliding occurs, leading to the instantaneous fracture of the top layer due to stress concentration.

3.5.2. *Microstructure evolution*

TEM structural characterization was conducted on the Ti/TiAlN coatings (Fig. 10(f)) after compression to investigate the strengthening mechanisms of the multilayer coating. The low-magnification TEM morphology is shown in Fig. 11(a), while the HRTEM morphology near the ductile layer, along with corresponding EDS and line scan results, is presented in Fig. 11(b). It is observed that the interface of the multi-layer structure remains distinct after compression. The variation in thickness of the ductile layer is related to stress concentration during the deformation process and the slight sliding of the top ceramic layer along the interface. HRTEM images of the plastic extrusion area (Fig. 11(c)) indicate that the Ti/TiAlN structure maintains its characteristic equiaxed composite columnar crystals. High-density dislocations are observed in the severely deformed regions of the Ti layer. The presence of the Ti-TiAlN multilayer heterogeneous interface effectively inhibits dislocation motion, promoting the accumulation of dislocations within the Ti layer [46,47]. The generation of dislocations during the deformation process absorbs strain energy, increasing the stress required for further plastic deformation [48].

Fig. 11(d) presents an HRTEM image of the Ti-TiAlN interface, showing specific orientation relationships during substantial grain deformation. According to the crystal band axis law, the $[11\bar{2}0]$ and [0001] crystal band axes exhibit a vertical orientation relationship. The crystal band axes in different directions appear simultaneously due to the rotation of crystal grains under high stress, resulting in altered crystal orientation. Fig. 11(e) illustrates the grain boundary formed by the parallel $[\bar{2}110]$ and $[10\bar{1}1]$ crystal band axes in high-resolution mode. Under complex stress states, externally applied stress induces lattice distortion within the crystal, causing crystallographic zone axes in various directions to appear simultaneously. Fig. 11(f) shows typical $\{01\bar{1}\bar{2}\}$ twins in the ductile layer. Twin boundaries, highlighted by red lines, as well as the traces of the matrix and twins, marked by yellow and green dashed lines, respectively, are observed. A mutually perpendicular relationship between the matrix and the twins is noted. At this point, the basal planes and prismatic planes of the grains on

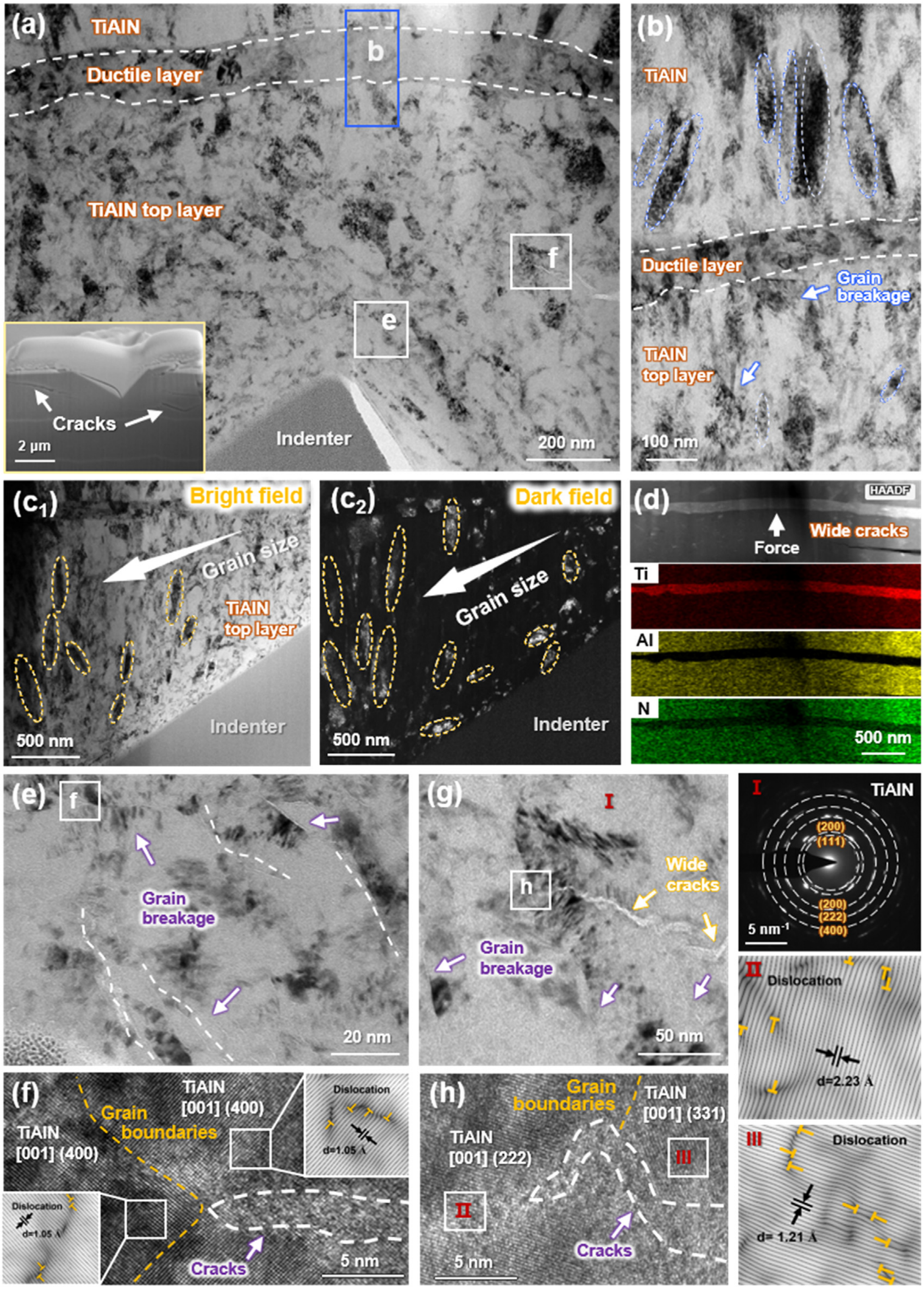

Fig. 12. Structural characterization of the coating under the indentation: (a) cross-sectional morphology, (b) crystal structure characteristics near the ductile layer after deformation, (c) grain refinement of deformed regions in bright and dark field modes, and (d) morphological characteristics and EDS mappings of the ductile layer after stress buffering; (e, f) grain-penetrating extension of microcracks under the indentation, and (g, h) grain-boundary extension of cracks under the indentation.

both sides became parallel, forming basal prismatic/prismatic basal (BP/PB) steps [49,50]. The twin boundaries themselves consist of short BP/PB steps and (0002) twin planes, which causes the twin orientations to deviate from theoretical predictions [51]. The SAED images of the twins demonstrate that the matrix and twins share diffraction spots, indicating a coherent structural relationship. The generation of deformation twins plays a crucial role in reducing the strain energy caused by deformation. Furthermore, it also enhances the plasticity and ductility of the material by inhibiting dislocation slip [52,53].

To elucidate the microcrack propagation mechanism of hard yet tough TiAlN-based multilayer coatings, Fig. 12 displays the cross-sectional characteristics of the coatings after 400 mN nanoindentation. The TEM cross-section morphology shown in Fig. 12(a) re-

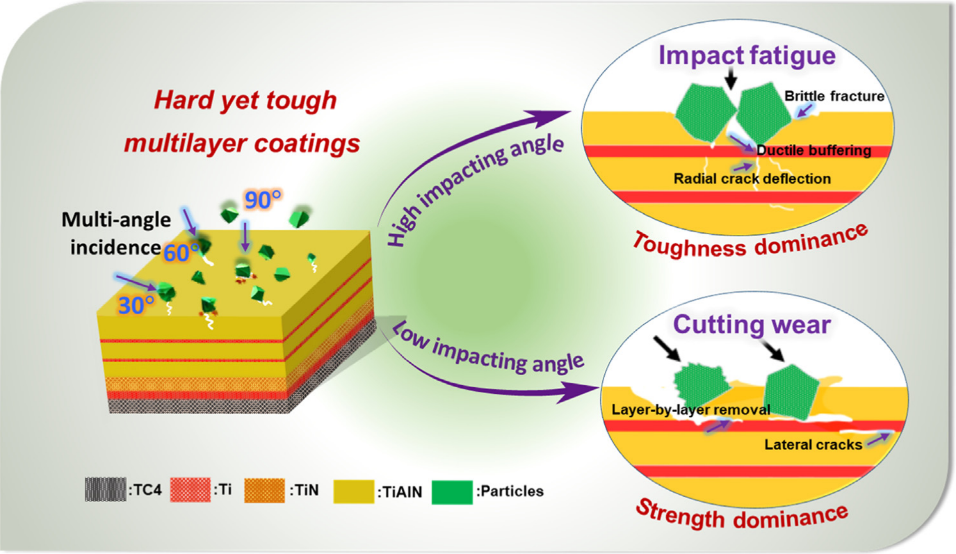

Fig. 13. Mechanism for improving the multi-angle erosion wear performance of Ti/TiAlN multilayer coatings.

veals that both plastic accumulation and crack growth occur to varying extents on either side of the indentation. Cracks primarily form on both sides of the indentation, with stress concentration alleviated through lateral cracking and radial extension. TEM results (Fig. 12(b)) near the ductile layer show that the Ti/TiAlN multilayer structure consists of alternating columnar and equiaxed crystals. In regions distant from the indenter, the TiAlN sublayer grains remain relatively intact, whereas the grain size in the TiAlN top layer, close to the indenter, appears significantly reduced. Fig. 12(c) further presents statistical analysis of the grain size of the TiAlN sublayer near the indenter, utilizing contrast imaging of bright and dark fields. It is clear that the grain size of the coating near the tip of the indenter is reduced, attributed to grain breakage under localized stress. During compression, grain refinement could absorb strain energy [54], and the ductile layer provides stress buffering through plastic deformation, thereby mitigating overall deformation. EDS analysis (Fig. 12(d)) further confirms that the ductile layer beneath the indentation, within the stress concentration zone, helps release stress and delay the onset of brittle cracking through coordinated deformation.

Fig. 12(e–h) illustrates the microcrack propagation under indentation, exhibiting both transgranular and intergranular modes. As is apparent in Fig. 12(e), a greater number of broken grains are observed beneath the indentation. The movement of dislocations within the crystal and their accumulation at the grain boundaries during compression make the deformed grain boundaries more apparent. In Fig. 12(f), the microcrack extends along the (400) plane under the [001] band axis. The crack propagates transgranularly but is obstructed by the grain boundary. Transgranular fracture, typically accompanied by plastic deformation, consumes significant energy via mechanisms such as dislocation motion. The tortuous expansion of microcracks requires overcoming resistance within the grains, further dissipating energy. Fig. 12(g) shows that the wider cracks initiate at both ends of the indentation and spread in a zigzag pattern within the ceramic layer. Fig. 12(h) demonstrates that the initial propagation of the microcrack along the grain boundaries of the (331) and (222) crystal faces of TiAlN is later blocked as the crack encounters the TiAlN (222) crystal faces. Crack propagation along the grain boundary dissipates less energy and occurs more rapidly than transgranular propagation, due to the relatively weak atomic bonds at grain boundaries. Under the action of various crack propagation modes, the plastic deformation ability of the material before failure is enhanced, and the toughness of the material is improved to a certain extent.

3.5.3. *Anti-erosion mechanism*

In order to elucidate the deformation behavior and performance enhancement mechanisms of hard yet tough Ti/TiAlN multilayer coatings under full-angle erosion, Fig. 13 presents a schematic representation of the damage behavior from a structural evolution perspective. It is evident that under low-angle erosion, particles interact with the coating surface in a manner resembling micro-cutting. The brittle ceramic layer exhibits micro-cracks as a result of damage and degradation, leading to layer-by-layer material removal as the interfacial bond strength diminishes under shear forces. The hard TiAlN sublayer at the top effectively resists the ploughing effect of the particles. In the case of high-angle erosion, particles impact the sample surface vertically, resulting in significant plastic deformation. In this instance, the multilayer structure, designed for enhanced toughness, prevents brittle spalling of the coating. Upon initiation and subsequent extension of a radial crack into the ductile metal layer, a degree of torsional bending occurs, which may have resulted in the crack closing. Concurrently, the metal layer absorbs strain energy through plastic flow during deformation, thereby alleviating stress concentrations.

4. Conclusions

In this work, hard yet tough Ti/TiAlN multilayer coatings were prepared by cathodic arc ion plating technology. The microstructural evolution and mechanisms of mechanical property enhancement were investigated through micropillar compression and foreign object damage tests. The following conclusions were drawn from the analysis:

(1) The alternating soft and hard laminated structure was found to enable the coatings to exhibit a balanced combination of strength and toughness. The coatings exhibited an adhesion strength of up to 72 N, a hardness of 25.1 GPa, and a modulus of 304.3 GPa.
(2) The coatings exhibited brittle material characteristics under full-angle erosion. The hard/ductile properties of coatings have been demonstrated to enhance resistance to low-angle cutting and high-angle fatigue damage prior to peeling off.

(3) The application of coatings resulted in a reduction of damage depth by over 20 % under both high-speed (350 m/s) and low-speed (250 m/s) glass bead impact. This demonstrates the superior resistance of the material to foreign object impact.

(4) During the fracture process, the ductile layers absorbed strain energy through mechanisms such as deformation twinning, dislocation generation, and cooperative deformation induced by grain rotation, thereby enhancing toughness. The dissipation of energy by the ceramic layers was achieved via grain refinement and mixed transgranular/intergranular crack propagation, thereby alleviating stress concentration.

Declaration of competing interest

The authors declare that they have no known competing financial interests or personal relationships that could have appeared to influence the work reported in this paper The author is an Editorial Board Member/Editor-in-Chief/Associate Editor/Guest Editor for *[Journal name]* and was not involved in the editorial review or the decision to publish this article.

CRediT authorship contribution statement

Jingjun Yan: Formal analysis, Writing – original draft, Investigation. **Yan Zhang:** Software, Writing – review & editing, Validation. **Yupeng Zhang:** Conceptualization, Methodology, Investigation. **Guanshui Ma:** Conceptualization, Supervision. **Shenghao Zhou:** Methodology, Funding acquisition. **Zhenyu Wang:** Writing – review & editing, Funding acquisition. **Aiying Wang:** Funding acquisition, Writing – review & editing, Supervision.

Acknowledgements

This work was financially supported by the National Science Foundation for Distinguished Young Scholars of China (No. 52025014), the National Natural Science Foundation of China (No. 52171090), the Natural Science Foundation of Zhejiang Province (No. LQ23E010002), and the Natural Science Foundation of Ningbo Municipality (Nos. 2023J410 and 2024Z154). The authors also want to give thanks to Nanjing University of Aeronautics and Astronautics for the air cannon impact test and Beihang University for the in situ compression test.

Supplementary materials

Supplementary material associated with this article can be found, in the online version, at doi:10.1016/j.jmst.2025.06.029.

References

[1] M.J. Presby, J.L. Stokes, B.J. Harder, J. Am. Ceram. Soc. 107 (2024) 1776–1792.
[2] D.W. Wheeler, R.J.K. Wood, Wear 9 (2024) 205488.
[3] B.D. Beake, S.R. Goodes, H. Zhang, L. Isern, C. Chalk, J.R. Nicholls, M.G. Gee, Tribol. Int. 195 (2024) 109647.
[4] D. Geng, H. Li, Z. Chen, Y.X. Xu, Q. Wang, J. Mater. Sci. Technol. 100 (2022) 150–160.
[5] X. Chen, R. Wang, N. Yao, A.G. Evans, J.W. Hutchinson, R.W. Bruce, Mater. Sci. Eng. A 352 (2003) 221–231.
[6] V. Bonu, M. Jeevitha, V.P. Kumar, G. Srinivas, H.C. Barshilia, Surf. Coat. Technol. 387 (2020) 125531.
[7] R. Tu, M. Jiang, M. Yang, B. Ji, B. Gao, S. Zhang, L. Zhang, Mater. Sci. Eng. A 866 (2023) 144696.
[8] V. Bonu, M. Jeevitha, V.P. Kumar, S. Bysakh, H.C. Barshilia, Appl. Surf. Sci. 478 (2019) 872–881.
[9] J. Ding, W. Tian, P. Zhang, M. Zhang, J. Chen, Y. Zhang, Z. Sun, J. Adv. Ceram. 8 (2019) 90–101.
[10] K.S. Selivanov, A.M. Smyslov, Y.M. Dyblenko, I.P. Semenova, Wear 418 (2019) 160–166.
[11] X. Zhang, R. Namakian, A.C. Meng, D. Moldovan, W.J. Meng, Mater. Sci. Eng. A 855 (2022) 143889.
[12] X. Zhang, B. Zhang, Y. Mu, S. Shao, C.D. Wick, B.R. Ramachandran, W.J. Meng, Acta Mater. 138 (2017) 224–236.
[13] L.W. Yang, C. Mayer, N. Li, J.K. Baldwin, N.A. Mara, N. Chawla, J.M. Molina-Aldareguia, J. Llorca, Acta Mater. 142 (2018) 37–48.
[14] L. Zhang, Y.Q. Shen, Y.M. Zhao, S.N. Chen, X. Ouyang, X. Zhang, H. Liang, B. Liao, L. Chen, Surf. Interfaces 38 (2023) 102836.
[15] V. Bonu, S. Kumar, P.N. Sooraj, H.C. Barshilia, Mater. Des. 198 (2021) 109389.
[16] E. Bousser, L. Martinu, J.E. Klemberg-Sapieha, Surf. Coat. Technol. 257 (2014) 165–181.
[17] J. Shuai, X. Zuo, Z. Wang, P. Guo, B. Xu, J. Zhou, A. Wang, P. Ke, Ceram. Inter. 46 (2020) 6672–6681.
[18] H. Ruan, Z. Wang, L. Wang, L. Sun, H. Peng, P. Ke, A. Wang, Surf. Coat. Technol. 438 (2022) 128419.
[19] D. Zhou, Z. Wang, Y. Zhang, J. Yan, G. Ma, X. Hu, P. Ke, A. Wang, Corros. Sci. 222 (2023) 111431.
[20] J. Yan, Z. Wang, S. Zhou, G. Ma, D. Zhou, W. Yang, A. Wang, Surf. Coat. Technol. 490 (2024) 131187.
[21] J. Shuai, X. Zuo, Z. Wang, L. Sun, R. Chen, L. Wang, A. Wang, P. Ke, J. Mater. Sci. Technol. 80 (2021) 179–190.
[22] W. Zhang, A. Chabok, H. Wang, J. Shen, J.P. Oliveira, S. Feng, N. Schell, B.J. Kooi, Y. Pei, J. Mater. Sci. Technol. 187 (2024) 195–211.
[23] J.I. Jang, G.M. Pharr, Acta Mater. 56 (2008) 4458–4469.
[24] S. Zhang, D. Sun, Y. Fu, H. Du, Surf. Coat. Technol. 198 (2005) 74–84.
[25] R. Wei, C. Rincon, E. Langa, Q. Yang, J. Vac. Sci. Technol. A 28 (2010) 1126–1132.
[26] V. Bonu, M. Jeevitha, V. Praveen Kumar, G. Srinivas, H.C.B. Siju, Surf. Coat. Technol. 387 (2020) 125531.
[27] K. Chu, K. Yan, F. Ren, Q. Sun, Scri. Mater. 172 (2019) 138–143.
[28] S. Shim, H. Bei, M.K. Miller, G.M. Pharr, E.P. George, Acta Mater. 57 (2009) 503–510.
[29] D. Kiener, C. Motz, M. Rester, M. Jenko, G. Dehm, Mater. Sci. Eng. A 459 (2007) 262–272.
[30] F. Xiao, K. Chu, Z. Li, R. Hou, Y. Gao, Q. Sun, X. Jin, Int. J. Plast. 160 (2023) 103480.
[31] A.N. Panckow, J. Steffenhagen, B. Wegener, L. Dübner, F. Lierath, Surf. Coat. Technol. 138 (2001) 71–76.
[32] M. Simsir, Y. Palaci, A. Özer, J. Aust. Ceram. Soc. 57 (2021) 1027–1037.
[33] A.R. Shugurov, M.S. Kazachenok, Surf. Coat. Technol. 353 (2018) 254–262.
[34] Y. Xie, H.M. Hawthorne, Surf. Coat. Technol. 155 (2022) 121–129.
[35] J.Y. Zhang, X. Zhang, R.H. Wang, S.Y. Lei, P. Zhang, J.J. Niu, G. Liu, G.J. Zhang, J. Sun, Acta Mater. 59 (2011) 7368–7379.
[36] T. Schlech, S. Horn, C. Wijayawardhana, A. Rashidi, J. Adv. Ceram. 10 (2021) 139–151.
[37] K. Luo, S. Xu, L. Xu, Y. Xing, H. Zhang, C. Wang, J. Lu, Surf. Coat. Technol. 481 (2024) 130608.
[38] W.J. Jo, H.J. Ahn, J.H. Kim, D. Kwon, J. Mater. Sci. Technol. 32 (2016) 1204–1210.
[39] M. Liu, Z. Xu, J. Adv. Ceram. 12 (2023) 1136–1165.
[40] X. Zhang, F. Li, Y. Li, Q. Lu, Z. Li, H. Lu, X. Ran, X. Qi, Surf. Coat. Technol. 403 (2020) 126366.
[41] A.A. Cenna, N.W. Page, E. Kisi, M.G. Jones, Wear 271 (2011) 1497–1503.
[42] B.D. Beake, Coatings 12 (2022) 793.
[43] J.O. Peters, R.O. Ritchie, Mater. Sci. Eng. A 319 (2001) 597–601.
[44] J.M. Wheeler, C. Harvey, N. Li, A. Misra, N.A. Mara, X. Maeder, J. Michler, S. Pathak, Mater. Sci. Eng. A 804 (2021) 140522.
[45] R. Raghavan, J.M. Wheeler, D. Esqué-De los Ojos, K. Thomas, E. Almandoz, G.G. Fuentes, J. Michler, Mater. Sci. Eng. A 620 (2015) 375–382.
[46] S.H. Li, Y. Zhao, P. Kumar, U. Ramamurty, Mater. Sci. Eng. A 851 (2022) 143591.
[47] A.S. Schneider, D. Kiener, C.M. Yakacki, H.J. Maier, P.A. Gruber, N. Tamura, M. Kunz, A.M. Minor, C.P. Frick, Mater. Sci. Eng. A 559 (2013) 147–158.
[48] H. Wang, M. Deng, Z. Huang, K. Lu, J. Shen, H. Qian, Z. Huang, J. Qi, Q. Wang, J. Adv. Ceram. 13 (2024) 1566–1577.
[49] H.C. Wu, Y.X. Yu, X.F. Bi, Trans. Nonferrous Met. Soc. China 28 (2018) 1538–1542.
[50] J. Wang, L. Liu, C.N. Tomé, S.X. Mao, S.K. Gong, Mater. Res. Lett. 1 (2013) 81–88.
[51] B. Xu, L. Capolungo, D. Rodney, Scr. Mater. 68 (2013) 901–904.
[52] S. Zhao, R. Zhang, Q. Yu, J. Ell, R.O. Ritchie, A.M. Minor, Science 373 (2021) 1363–1368.
[53] Y. Zhang, Y. Hou, H. Zheng, L. Zhao, S. Jia, K. Li, H. Peng, P. Zhao, L. Li, W. Meng, R. Jiang, J. Mater. Sci. Technol. 135 (2023) 231–240.
[54] Z. Huang, Y. Shi, Y. Zhang, M. Deng, Y. Guo, Q. Kong, J. Qi, B. Ma, Q. Wang, H. Wang, J. Adv. Ceram. 11 (2022) 1976–1987.